Taylor & Francis
Taylor & Francis Group

A Model of the Structural and Functional Development of the Normal Human Fetal Left Ventricle Based on a Global Growth Law

JACQUES OHAYON[a],*, HONGXUE CAI[b], PIERRE-SIMON JOUK[c], YVES USSON[c] and ANNABELLE AZANCOT[d]

[a]*Department of Composite Materials, LaMaCo, Engineering School of Chambery, University of Savoie, 73376 Le Bourget du Lac, France;* [b]*Laboratory of Cellular Biology/NIDCD, National Institutes of Health, Bethesda, MD 20892, USA;* [c]*Pattern Recognition and Quantitative Microscopy, UMR CNRS 5525, Université Joseph Fourier, BP 217, 38043 Grenoble Cedex 9, France;* [d]*Robert Debré hospital, Perinatal Cardiology and Physiology, 48 Blvd. Serurier, 75019 Paris, France*

The purpose of this research is to study the growth of the normal human left ventricle (LV) during the fetal period from 14 to 40 weeks of gestation. A new constitutive law for the active myocardium describing the mechanical properties of the active muscle during the whole cardiac cycle has been proposed. The LV model is a thick-walled, incompressible, hyperelastic cylinder, with families of helicoidal fibers running on cylindrical surfaces [1]. Based on the works of Lin and Taber [2] done on the embryonic chick heart, we use for the human fetal heart a growth law in which the growth rate depends on the wall stresses. The parameters of the growth law are adapted to agree with sizes and volumes inferred from two dimensional ultrasound measurements performed on 18 human fetuses.

Then calculations are performed to extrapolate the cardiac performance during normal growth of the fetal LV. The results presented support the idea that a growth law in which the growth rate depends linearly on the mean wall stresses averaged through the space and during whole cardiac cycle, is adapted to the normal human fetal LV development.

Keywords: Human fetus; Growth; Constitutive law; Myocardium; Myocardial fiber orientation; Left ventricle; Mathematical model; Finite deformations

INTRODUCTION

The differentiation and growth of the heart are governed by two sets of factors: those that are genetic (time-dependent) and those that are epigenetic (function-dependent). The first set is mainly effective during the very first stages of the embryonic cardiac development. During most of life, however, the growth of the heart is closely matched to its functional load [3,4].

Due to the poor availability of experimental data, no biomechanical model attempts to simulate the growth of the normal human heart during the fetal period. The work of Lin and Taber [2], using the theory of Rodriguez *et al.* [5] for finite tissue growth, suggests that wall stress may be a reasonable biomechanical factor that regulates growth in the heart. Their model for stress-induced growth in the developing heart was applied to the embryonic chick LV, and assumed that the rate of growth depends only on

the end-diastolic stresses and that the myocardium is isotropic.

However, the cardiac muscle tissue, or myocardium, is a complex structure composed primarily of cardiac muscle cells arranged in a more or less parallel weave. Each cell has several branches to other cells, but nonetheless a sense of direction or grain is preserved. We shall denote the local grain direction by the unit vector **t** and refer to it also as the local "fiber" direction with the understanding that individual continuous muscle fibers do not really exist. The study of the topological organization of myocardial cells is a basic requirement for the understanding of the mechanical design of the normal and pathological human fetal heart. Anatomical observations show that, in the human, the adult cardiac muscle tissue [6–10] as well as the normal fetal myocardium [1,11–14] have a highly specialized fiber architecture.

---

*Corresponding author. Tel.: +(33) 479 75 8604, Fax: (33) 479 75 8772, E-mail: jacques.ohayon@univ-savoie.fr

TABLE I Distribution of the population according to gestational age (GA in weeks) and of the end-diastolic echocardiographic studies. The normal length of the human gestation is 41 weeks. F_i ($i = 1, \ldots, 18$) : are the eighteen fetal hearts analyzed. V_{int}: LV cavity volume, L_{int}: Internal major-axis, L_{ext}: External major-axis, r_{int}: Internal equatorial radius, r_{ext}: External equatorial radius, V_{myo}: Myocardial volume. The mean gestational age at the time of the study is 28 weeks

Study, GA	V_{int} (ml)	L_{int} (cm)	L_{ext} (cm)	r_{int} (cm)	r_{ext} (cm)	V_{myo} (ml)
F1, 20 w	0.421	1.367	1.558	0.318	0.439	0.487
F2, 20 w	0.182	1.716	2.003	0.234	0.452	0.765
F2, 26 w	1.707	2.296	2.879	0.502	0.812	3.119
F3, 20 w	0.470	1.628	1.991	0.328	0.529	1.045
F3, 36 w	3.380	2.310	2.831	0.773	1.143	6.170
F4, 21 w	0.259	1.056	1.227	0.301	0.478	0.467
F5, 21 w	0.290	1.486	1.649	0.287	0.444	0.432
F5, 28 w	2.082	2.154	2.500	0.660	0.888	2.834
F5, 35 w	2.432	3.074	3.645	0.579	0.964	5.267
F6, 21 w	0.273	1.414	1.538	0.271	0.423	0.372
F6, 33 w	1.801	2.037	2.256	0.488	0.657	1.784
F7, 22 w	0.761	2.032	2.272	0.328	0.466	1.075
F7, 27 w	1.395	1.795	2.046	0.482	0.677	1.337
F7, 35 w	2.193	2.488	2.727	0.627	0.814	2.345
F7, 37 w	4.010	2.971	3.344	0.662	1.104	6.222
F8, 24 w	0.653	1.441	1.715	0.464	0.701	1.105
F8, 27 w	0.678	2.003	2.387	0.321	0.653	1.999
F8, 37 w	4.912	3.186	3.566	0.735	1.020	4.895
F9, 24 w	0.721	1.810	2.186	0.376	0.659	1.861
F9, 30 w	2.117	2.719	2.993	0.555	0.781	2.582
F10, 25 w	0.865	1.669	2.076	0.450	0.663	1.462
F11, 25 w	0.448	1.643	1.851	0.357	0.527	0.699
F11, 29 w	1.587	2.268	2.558	0.536	0.873	3.055
F12, 25 w	0.337	1.302	1.569	0.290	0.534	0.930
F12, 33 w	3.405	3.119	3.530	0.655	0.926	4.860
F13, 27 w	1.027	3.041	3.390	0.403	0.679	2.526
F14, 27 w	1.676	2.525	3.006	0.525	0.837	2.670
F15, 28 w	2.658	2.002	2.233	0.635	0.920	2.810
F15, 33 w	2.57	1.864	2.282	0.691	1.011	3.120
F15, 34 w	2.631	2.608	3.035	0.552	0.958	4.741
F16, 29 w	0.418	1.751	2.165	0.356	0.627	1.389
F16, 35 w	3.369	2.558	2.973	0.771	1.027	3.541
F17, 33 w	1.093	2.253	2.460	0.395	0.652	1.632
F18, 34 w	3.655	2.278	2.806	0.699	0.980	4.073

Several clinical studies currently exist that attempt to measure the change of ventricular geometry and cavity volumes of the human heart during the fetal life [15–17]. Nevertheless, these studies did not provide LV mass and wall thickness, which are required to simulate the growth of the human fetal LV. In our study, LV mass, diameters, and wall thickness was evaluated in 18 normal human fetal hearts.

From our anatomical and clinical data obtained on the human fetuses, we have developed a model for stress-induced growth in the developing human fetal LV where: (i) the myocardium is an anisotropic medium, (ii) the new suggested constitutive law for the active myocardium makes it possible to simulate continuously the LV behavior during the whole cardiac cycle, (iii) the growth rate depends linearly on the mean stresses averaged through the ventricular wall and during the whole cardiac cycle, and (iv) the coefficients of the postulated growth law are adapted to fit the clinical data.

Then simulations are run on LV in normal condition, and the resulting performances are analyzed.

DETERMINATION OF LV VOLUME, MASS AND GEOMETRY IN NORMAL HUMAN FETUSES BY TWO-DIMENSIONAL ECHOCARDIOGRAPHY

Population and Methods

Population

The research study was approved by the Human Investigation Committee of our institution. We studied 18 fetuses noted F_i, $i = 1$ to 18 (11 of which were analyzed at least twice), from 20 to 37 weeks of gestation. Gestational age was estimated by sonographic study in the first trimester and or measurements of fetal biparietal diameter and femoral length during the second trimester according to the norms of our laboratory. The pregnancies were normal as well as the clinical postnatal control of the neonates. Table I gives the population used and shows the distribution of gestational age for the 34 two-dimensional echocardiographic (2DE) studies performed on 18 fetuses.

Analysis of Imaging

Fetal hearts were examined using an Acuson 128 variable focus ultrasound system with a 5 or 3.5 MHz sector transducer. A complete examination of the fetal heart was performed using cross-sectional imaging and spectral Doppler to confirm a normal fetal heart anatomy. The examinations were recorded on video tape for off-line analysis. Analysis of 2DE recording was performed using a computer-assisted analysis system and commercially available software (UN-SCAN-IT, Silk Scientific, Utah, USA). End-diastolic frames from the LV in apical two-chamber view were selected and digitized. To select appropriate frames for analysis, cine-loop acquired image were carefully observed over several cardiac cycles. The frame at atrioventricular valve closure was defined as the end-diastolic frame. Alternatively, when the precise points of valve closure could not be clearly identified, frames that reflected the largest ventricles were selected. The septum, endocardium and epicardium of the LV were traced and a Simpson's rule algorithm using thirty cords (n = 30) was used to calculate LV cavity and external volumes (noted respectively V_{int} and V_{ext}) (Fig. 1)

$$V_{int} = \frac{\pi}{4}\sum_{i=1}^{n} a_i^2 \frac{L_{int}}{n}, \quad V_{ext} = \frac{\pi}{4}\sum_{i=1}^{n} A_i^2 \frac{L_{ext}}{n} \quad (1a, b)$$

where L_{int} and L_{ext} are the internal and external major-axis lengths measured from the endocardial-apical point and epicardial-apical point to the point between the aorta and the mitral valves, respectively. The Simpson's rule is based on the summation of n disks of equal height. The parameters a_i and A_i ($i = 1$ to n) in the Eqs. (1a) and (1b) are the internal and external diameters of the ith disk respectively and are defined in Fig. 1. The myocardial mass (M_{myo}) is then obtained from the myocardial volume ($V_{myo} = V_{ext} - V_{int}$) using the formula $M_{myo} = \rho_{myo} V_{myo}$ where ρ_{myo} is the volumic density of the myocardium
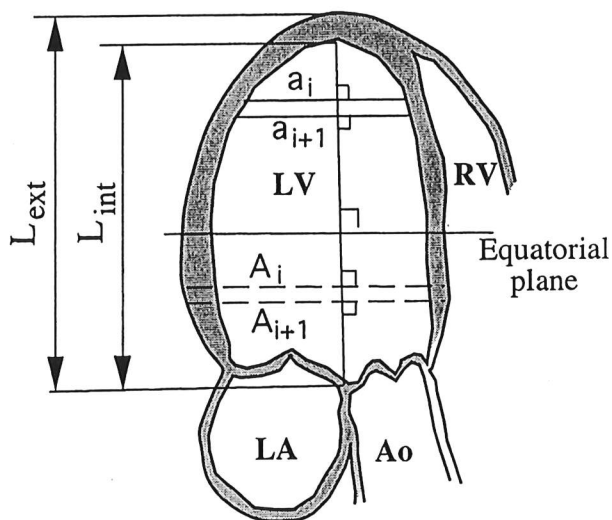
FIGURE 1 Schematic representation of the apical two-chamber view of the human fetal heart. LV: left ventricle, RV: right ventricle, LA: left atrium, Ao: Aorta, A_i and a_i ($i = 1, \ldots, n$) correspond to the measured diameters, L_{int}: internal long-axis, L_{ext}: external long-axis.

FIGURE 3 Measured and computed end-diastolic LV internal long-axis during the normal human fetal life. We compare our sequential measurements to those of McCaffrey et al. (1997), and the best fit of our data is compared to the model predicted values. The open circles correspond to our data given in Table I.

almost constant during fetal life [3] and equal to 1.05×10^{-3} kg/ml. We have also measured, at end-diastole, the internal diameter ($2r_{int}$) and external diameter ($2r_{ext}$) at the equatorial level of the LV for every fetal hearts. The equatorial plane is the plane perpendicular to the major-axis at the level of the mid-internal major-axis (Fig. 1).

Comparison and Clinical Results

Comparison

The 2DE determination of the end-diastolic, LV cavity volumes (V_{int}), internal long-axis (L_{int}) and internal

equatorial radius (r_{int}) were compared with those obtained on human LV by Schmidt et al. [16] and by McCaffrey et al. [17] (Figs. 2–4). McCaffrey et al. [17] calculate the LV cavity volume from the apical four-chamber view and Schmidt et al. [16] from two orthogonal apical views which are the two-chamber and the four-chamber views. The latter validate their volume calculations on fetal lambs, by comparing the 2DE methods to the cast volumes of these ventricles [18]. Figure 2 compares calculated end-diastolic LV cavity volumes obtained by Schmidt et al. [16] and McCaffrey et al. [17] with ours. Figures 3 and 4 compare measured end-diastolic LV internal major-axis and internal equatorial radius obtained by McCaffrey et al. [17] with our data. Our measurements and volume
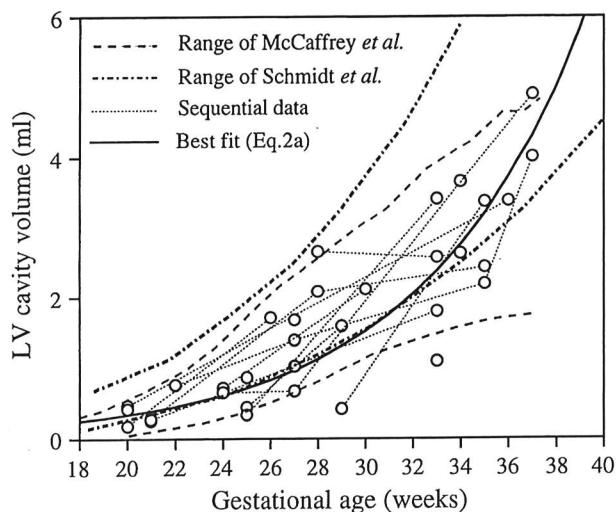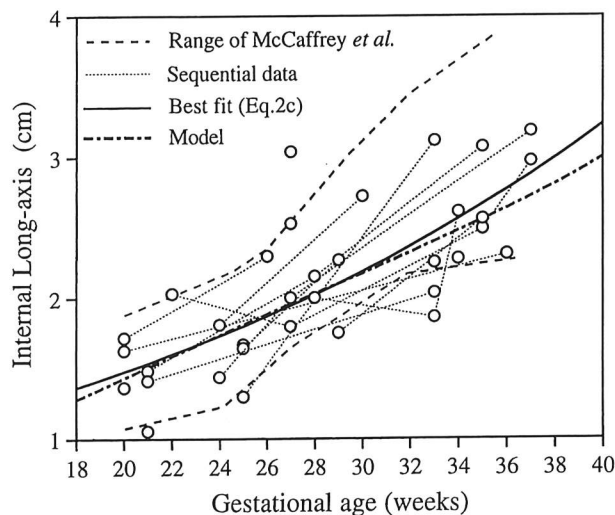

FIGURE 2 Measured and computed end-diastolic LV cavity volume during the normal human fetal life. We compare our sequential measurements to those of McCaffrey et al. (1997) and Schmidt et al. (1995). The best fit of our data is also presented. The open circles correspond to our data given in Table I.
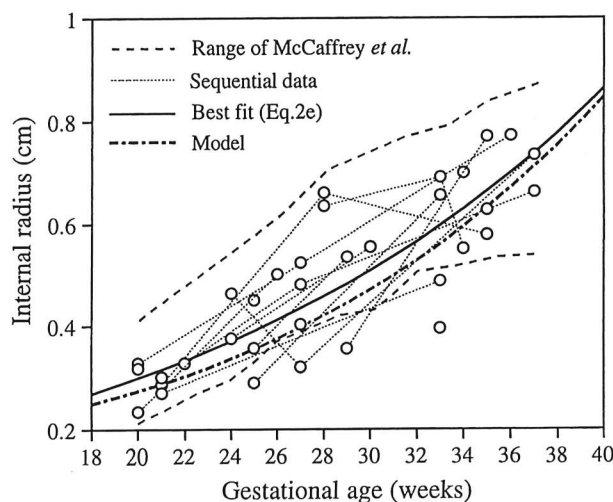

FIGURE 4 Measured and computed end-diastolic LV internal radius during the normal human fetal life. We compare our sequential measurements to those of McCaffrey et al. (1997), and the best fit of our data is compared to the model predicted values. The open circles correspond to our data given in Table I.
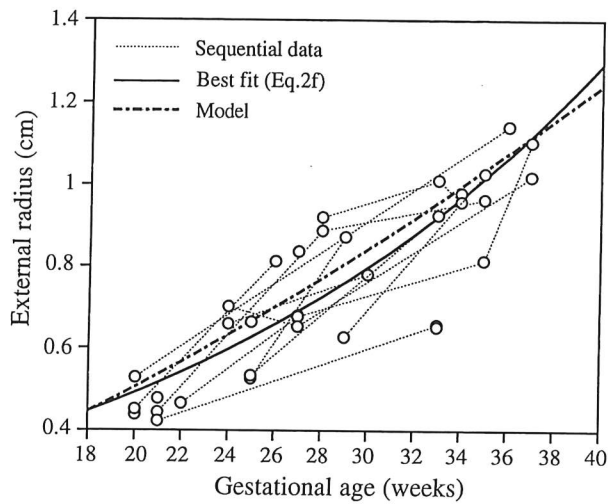
FIGURE 5   Measured and computed end-diastolic LV external radius during the normal human fetal life. The best fit of our data is compared to the model predicted values. The open circles correspond to our data given in Table I.
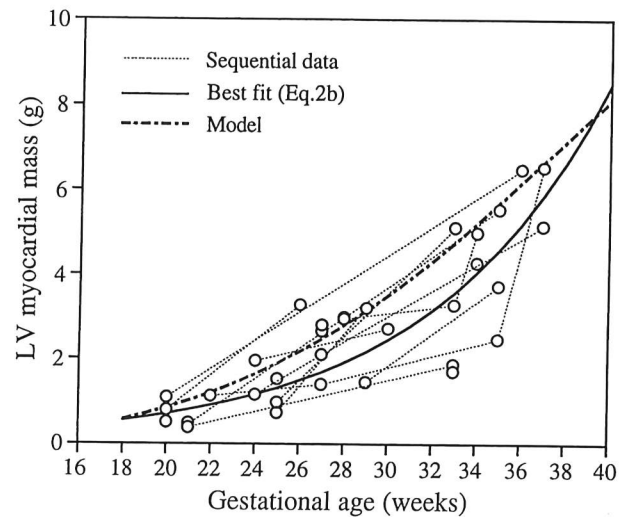

FIGURE 6   Measured and computed end-diastolic LV myocardial mass during the normal human fetal life. The best fit of our data is compared to the model predicted values. The open circles correspond to our data given in Table I.

calculations are in agreement with those of the previous authors. We did not find values concerning the major-axes and the equatorial radii from Schmidt *et al.* [16,19] in their published data. Figures 5 and 6 illustrate the change of the LV external equatorial radius (r_{ext}) and myocardial mass (M_{myo}), measured at end-diastole and during fetal life.

Intraobserver Variability

To test the variability in volume calculations from 2DE (V_{int} and V_{ext}), major-axis lengths (L_{int} and L_{ext}) and radii (r_{int} and r_{ext}) measurements, 5 randomly selected echocardiographic calculations and measurements were repeated. Variability was expressed as difference from the mean of the two results in percent of the mean. We get a variability of 5.5%, 11.7%, 11.7%, 6.8%, 8.2% and 1.7% for V_{int}, V_{myo}, L_{int}, L_{ext}, r_{int} and r_{ext} respectively.

Results

The fetal ultrasound measurements and calculations are presented in Table I. The best regression equations found for the end-diastolic, LV cavity volume (V_{int}), myocardial volume (V_{myo}), internal major-axis (L_{int}), external major-axis (L_{ext}), internal equatorial radius (r_{int}) and external equatorial radius (r_{ext}) were:

$$V_{int} = 0.017 \times 10^{0.065tg} \quad r = 0.87 \,(\text{unit}:\text{ml}) \quad (2a)$$

$$V_{myo} = 0.056 \times 10^{0.054tg} \quad r = 0.85 \,(\text{unit}:\text{ml}) \quad (2b)$$

$$L_{int} = 0.676 \times 10^{0.017tg} \quad r = 0.77 \,(\text{unit}:\text{cm}) \quad (2c)$$

$$L_{ext} = 0.795 \times 10^{0.017tg} \quad r = 0.77 \,(\text{unit}:\text{cm}) \quad (2d)$$

$$r_{int} = 0.104 \times 10^{0.023tg} \quad r = 0.84 \,(\text{unit}:\text{cm}) \quad (2e)$$

$$r_{ext} = 0.187 \times 10^{0.021tg} \quad r = 0.87 \,(\text{unit}:\text{cm}) \quad (2f)$$

where t_g is the growth time or gestational age in weeks, and r is the correlation coefficient.

MAPPING OF THE ORIENTATION OF MYOCARDIAL CELLS BY POLARIZED LIGHT MICROSCOPY IN LATERAL WALL OF THE NORMAL HUMAN FETAL LV

Quantitative measurements of fiber orientation through the heart wall by means of polarized light analysis [20,21] on some thick sections of normal human fetal heart embedded in a resin and polymerized have been made by Ohayon *et al.* [1] and Jouk *et al.* [14]. A complete three-dimensional cartography of the pattern of the myofibers in the second trimester fetal human heart has been established by Jouk *et al.* [14]. Their data base (18 hearts aged 14 to 27 weeks of gestation) (i) shows that at the beginning of the fetal period the endocardial trabeculated muscle account for no more than 15% of the gross myocardial volume, and (ii) supports the assumption of transverse isotropy of the myocardium at the fetal stage. The previous work [1] concerns three normal human fetal hearts (FH) of 14, 20 and 33 weeks of gestational age. For every heart, a series of thick sections (500 μm), transverse with reference to the base to apex axis, was cut. At a given myocardial *point* (or voxel which is an elementary volume of 130 × 130 × 500 μm), the elevation angle (or helicoidal angle) γ with reference to the plane of the section is measured. This angle γ is the angle of the fiber with the section plane. All their measurements are made in the lateral wall of the fetal LV. For the three FH, the variation of the elevation fiber angle from the endocardial to the epicardial surfaces in the lateral wall are measured in each transverse sections. From their observations they can extract two anatomical features in the lateral wall of their three fetal LV: (i) in one FH
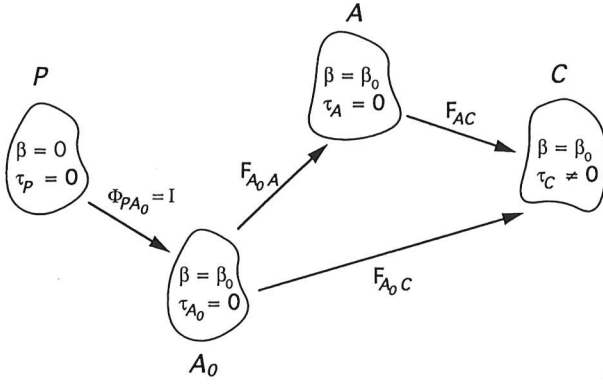
FIGURE 7 Description of the active rheology approach. The activation of the muscle sample is a combination of two transformations. The first one, changes only the material properties without changing the geometry of the sample (from state P to state A_0), then the second one contracts the muscle without changing the rheology (from state A_0 to state A). At the end, loading is applied (from state A to state C). We use the symbol Φ for a non elastic transformation and the letter F for an elastic transformation. β is the activation function ($\beta = 0$ at end-diastole and $\beta = 1$ at end-systole) and τ is the Cauchy's stress tensor.

the observed variations of the endocardial to epicardial distributions of the elevation angle from base to apex were small. Therefore they use, for the normal FH, a mean radial distribution of γ (noted $\gamma_{\text{nor.}}$), and (ii) the mean radial distributions of the elevation angle form endocardial to epicardial surfaces between the three FH are quite the same. Their best fit of this distribution is given by the equation $\gamma_{\text{nor.}}(\rho) = -55(e^{12(\rho-0.5)} - 1)/(e^{12(\rho-0.5)} + 1)$ (Fig. 4B in Ohayon et al. [1]) where $\gamma_{\text{nor.}}$ is in degree and ρ is the normalized radial position in the wall with $\rho = 0$ at the endocardium and $\rho = 1$ at the epicardium, $0 \leq \rho \leq 1$.

MECHANICAL MODEL FOR THE DEVELOPING NORMAL HUMAN FETAL LV

In this model of structural and functional development of the normal human fetal LV, the following assumptions are made:

  i) The active and passive material properties remain constant during fetal life.
 ii) Only radial, circumferential and longitudinal growth of the fetal LV are considered.
iii) The muscle activation amplitudes and the time phases in the cardiac cycle do not change during fetal life.
 iv) The kinematics of the LV growth allows only radial displacement of the LV base and the apex is free to move.

Left Ventricular Geometry and Fiber Organization at the Initial Time of Growth

Let P_0 and S_0, denote the passive stress-free state and the passive unloaded physiological state of the human fetal

LV at the beginning of the fetal life ($t_g = t_0$), respectively. To keep the problem mathematically tractable, we have made three major assumptions on the geometry of the LV and fiber organization at the initial growth time, corresponding to 14 weeks of gestation in our study:

  i) The passive stress-free geometry of the LV (state P_0) is approximated by a thick-walled open cylinder of length L_{P_0}, internal radius $R_{i_{P_0}}$, external radius $R_{e_{P_0}}$ and opening angle $\Theta_{P_0}^{\text{open}}$. In fact we assumed that the equatorial region of the LV drives the cardiac performance.
 ii) We neglected the penetration angle by assuming that the fibers are running on cylindrical shells of revolution. It has been shown [1,22,23] that this angle affects mainly the LV torsion with almost no effect on the LV pressure-volume relation and that the elevation angle distribution is one of the major determinant of the cardiac performance.
iii) We assumed an axial symmetry of the elevation angle measured in the lateral wall of the LV at state S_0, and we used a same radial distribution of elevation angle invariant from base to apex given in Section 3 by $\gamma_{\text{nor.}}(\rho)$. Note that the previous radial distribution of γ_{S_0} (or $\gamma_{\text{nor.}}$) as well as the internal radius $R_{i_{S_0}}$, external radius $R_{e_{S_0}}$ and the length L_{S_0} are only given at the initial physiological state S_0. Then these geometrical parameters and the radial distribution change with the gestational age and become one output of the model.

Constitutive Relation for the Active Myocardium

To be consistent with our mathematical formulation, the letter Φ is used for non elastic gradient tensor and the letter F is used for elastic gradient tensor.

The activation of the muscle fibers changes the rheology of the material and at the same time contracts the muscle itself. To have a continuous elastic description during the activation of the myocardium, we used an approach similar to the one proposed by Chadwick [24], Ohayon and Chadwick [25], Humphrey and Yin [26], Guccione et al. [27], and Hunter [28]. From its passive zero-stress state P, the activation of the muscle fibers is modeled by the following two transformations (Fig. 7): the first one (from state P to virtual state A_0) changes the material rheology without changing the geometry, and the second one (from A_0 to A) contracts the muscle without changing the rheology of the material. Thus, the former is not an elastic deformation and is described by the gradient tensor $\Phi_{PA_0} = I$ where I is the identity matrix. In that first transformation, only the strain energy function is modified using an activation function $\beta(t)$, where t is the cardiac cycle time ($0\,\sec \leq t \leq 0.5\,\sec$). The second transformation is an elastic deformation caused by the active tension delivered by the fibers and is described by the gradient tensor F_{A_0A}. Finally, external loads are applied to
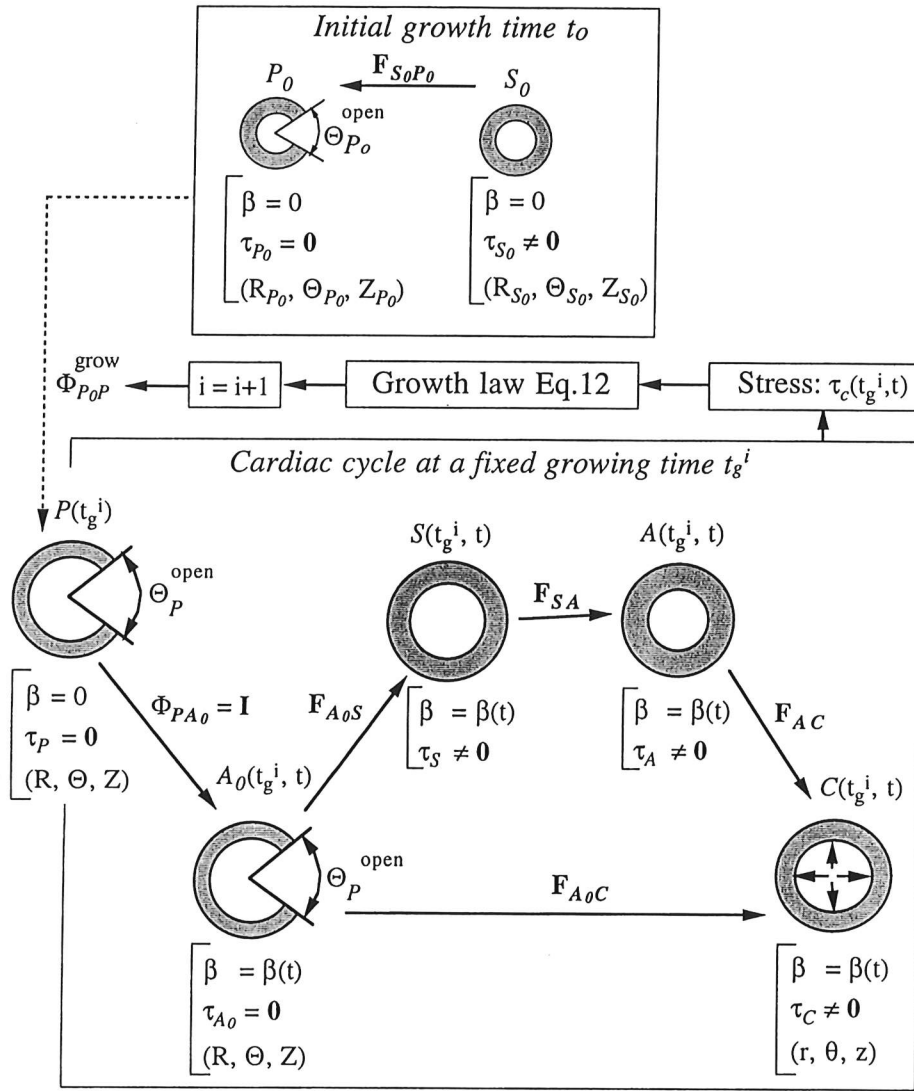
FIGURE 8   Description of the human fetal LV growth taking into account the cardiac cycle (see text for details).

state A deforming the body through $\mathbf{F}_{AC}$ into C. When the geometry of the muscle at state P is simple as a rectangular sample with unidirectional fibers, the state A is also free of stresses (Fig. 7). This is not the case for more complex structure made of different fiber layers as the fetal LV (Fig. 8).

The change of the material properties of the myocardium during the cardiac cycle is described by a time-dependent strain-energy function per unit volume of state P noted $W(\mathbf{E}_{PH}, t)$:

$$W(\mathbf{E}_{PH}, t) = W_{mat.}(\mathbf{E}_{PH}) + W^{f}_{pas.}(\mathbf{E}_{PH})$$

$$+ \beta(t)W^{f}_{act.}(\mathbf{E}_{PH}) \tag{3a}$$

where $\mathbf{E}_{PH}$ is the Green's strain tensor at an arbitrary state H calculated from the zero strain state P (the state H could be one of the states A_0, S, A or C shown in Figures 7 and 8), $W_{mat.}$ represents the contribution of the surrounding collagen matrix, $W^{f}_{pas.}$ and $W^{f}_{act.}$ arise from the passive and the active component of the embedded muscle fibers respectively, and $\beta(t)$ is an activation function equal to zero at end-diastolic state and equal to one at end-systolic state ($0 \leq \beta(t) \leq 1$). The third term of the right side of the Eq. (3a) gives the variation of the muscle fibers rheology during the cardiac cycle.

We treat the myocardium as a homogeneous, incompressible, and hyperelastic material transversely isotropic with respect to the local muscle fiber direction. This last direction is characterized in an arbitrary state H by the unit vector $\mathbf{t}_H$. In this study, the strain-energy functions are [29]:

$$W_{mat.}(\mathbf{E}_{PH}) = \frac{a}{b}(e^{b(I_1 - 3)} - 1) \tag{3b}$$

$$W^{f}_{pas.}(\mathbf{E}_{PH}) = \frac{a_f}{b_f}\{e^{b_f(I_4 - 1)} - 1 - b_f(I_4 - 1)\} \tag{3c}$$

$$W^{f}_{act.}(\mathbf{E}_{PH}) = \frac{c_f}{d_f}\left(I_4 + I_4^{-1} - 2\right)^{d_f} \tag{3d}$$

where a, b, a_f, b_f, c_f, d_f are material constants and I_1, I_4 are two strain invariants given by $I_1(\mathbf{E}_{PH}) = \mathrm{tr}\, \mathbf{C}_{PH}$ and $I_4(\mathbf{E}_{PH}) = \mathbf{t}_P \cdot \mathbf{C}_{PH} \mathbf{t}_P$ where $\mathbf{C}_{PH}$ is the right Cauchy-Green strain tensor ($\mathbf{C}_{PH} = 2\mathbf{E}_{PH} + \mathbf{I}$). Note that I_4 is directly related to the fiber extension $\lambda (I_4 = \lambda^2)$.

To incorporate the active contraction, an active fiber stress $\mathbf{T}^{(0)}$ was applied in the deformed fiber direction $\mathbf{t}_C$. Hence, during the cardiac cycle, the Cauchy stress tensor in state C (noted τ_C) is given by:

$$\tau_C = \mathbf{F}_{PC} \frac{\partial W(\mathbf{E}_{PC}, t)}{\partial \mathbf{E}_{PC}} \mathbf{F}_{PC}^T - p_C \mathbf{I} + \beta(t) T^{(0)} \mathbf{t}_C \otimes \mathbf{t}_C \quad (3e)$$

where p_C is the Lagrangian multiplier resulting of the incompressibility of the material [30–32], and the symbol $\otimes$ denotes the tensor product.

Description of the Human Fetal LV Growth

The growth of a tissue results of its cell division (hyperplasia) or enlargement (hypertrophy). Cardiac growth involves an increase in the number of myocardial cells (hyperplasia) through fetal life and continues until three months after birth in human [3]. After birth, hyperplasia is prominent initially, and then cell size increases (i.e., hypertrophies) with binucleation occurring [33]. Considering the cardiac cycle in the present growth model, it is necessary to point out that there are two time scales, the growth time (noted t_g) and the cardiac cycle time (noted t). The former may have a scale of hours or days, while the latter is less than a second. The growth flow-diagram is shown in Fig. 8. From state P_0, we simulate directly the cardiac cycle and calculate the cardiac stresses. Then these stresses affect the growth rate $\dot{\Phi}_{P_0P}^{\mathrm{grow}}$. The fetal LV undergoes volumetric growth while remaining stress-free, we therefore obtain the fetal LV state P at time $t_g = t_0 + \Delta t_g$ with an opening angle $\Theta_P^{\mathrm{open}}(t_0 + \Delta t_g)$. Then that state $P(t_0 + \Delta t_g)$ initializes a new cardiac cycle and so on.

Governing Equations

In this work, the cylindrical coordinates and their associated unit vectors in an arbitrary state H are noted (R_H, Θ_H, Z_H) and $(\mathbf{e}_{RH}, \mathbf{e}_{\Theta H}, \mathbf{e}_{ZH})$, respectively.

Kinematics of the LV Growth (tensor Gradient $\Phi_{P_0P}^{\mathrm{grow}}$)

We choose a simple kinematics of the LV growth, to keep mathematics tractable in the present model. Only radial, circumferential and longitudinal growth were considered, thus the cylindrical geometry of the LV is conserved, and no twist occurs during the growth process:

$$\Phi_{P_0P}^{\mathrm{grow}} = \alpha_R \mathbf{e}_{RP} \otimes \mathbf{e}_{RP_0} + \alpha_\Theta \mathbf{e}_{\Theta P} \otimes \mathbf{e}_{\Theta P_0}$$
$$+ \alpha_Z \mathbf{e}_{ZP} \otimes \mathbf{e}_{ZP_0} \quad (4a)$$

where

$$\frac{\partial R_P}{\partial R_{P_0}} = \alpha_R, \quad \frac{R_P}{R_{P_0}} \frac{\partial \Theta_P}{\partial \Theta_{P_0}} = \alpha_\Theta \quad \text{and} \quad \frac{\partial Z_P}{\partial Z_{P_0}} = \alpha_Z \quad (4b\text{–}d)$$

Moreover, we assumed that the growth stretch ratios α_i ($i = R$, Θ or Z) vary with t_g and have no spatial dependence. Then if we allow only radial displacement on the LV base (on $Z_{P_0} = 0$), the integration of the Eqs. (4b–d) gives:

$$R_p = \alpha_R R_{P_0}, \quad \Theta_P = \frac{\Theta_P^*}{\Theta_{P_0}^*} \Theta_{P_0}, \quad Z_P = \alpha_Z Z_{P_0} \quad (4e\text{–}g)$$

with

$$\Theta_P^* = \Theta_{P_0}^* \alpha_\Theta \alpha_R^{-1} \quad (4h)$$

where $R_{iP_0} \le R_{P_0} \le R_{ep_0}$, $-\Theta_{P_0}^* \le \Theta_{P_0} \le \Theta_{P_0}^*$ and $-L_{P0} \le Z_{P_0} \le 0$. The two angles Θ_P^* and $\Theta_{P_0}^*$ are related to the opening angle of the LV at state P (noted Θ_P^{open}) and P_0 (noted $\Theta_{P_0}^{\mathrm{open}}$), respectively, by the equations $\Theta_P^* = \pi - \Theta_P^{\mathrm{open}}/2$ and $\Theta_{P_0}^* = \pi - \Theta_{P_0}^{\mathrm{open}}/2$. Note if $\alpha_\Theta \alpha_R^{-1} = 1$ then the opening angle at initial stress-free state P_0 stays the same at stress-free state P (i.e., $\Theta_P^* = \Theta_{P_0}^*$). In addition, if the cylinder at state P_0 is closed ($\Theta_{P_0}^* = \pi$) then the growth strain is geometrically compatible [34] and the LV stays a closed cylinder at state P ($\Phi_{PS} = \mathbf{I}$ in Fig. 8).

With such a kinematics (Eqs. (4e–h)) a same fiber runs always on cylinder shells and the unit vector in the fiber direction is given by $\mathbf{t}_p = \cos \gamma_P \mathbf{e}_{\Theta P} + \sin \gamma_P \mathbf{e}_{ZP}$ where γ_P is the radial distribution of the elevation angle at state P. The relation between γ_P and the radial distribution of the elevation angle at state P_0 (noted γ_{P_0}) is given by the equation (see appendix part B):

$$\gamma_p = \arctan(\alpha_\Theta^{-1} \alpha_Z \tan \gamma_{P_0}) \quad (4i)$$

Because the radial distribution γ is only known at passive unloaded physiological state S_0, it is useful to write γ_{P_0} as a function γ_{S_0} (see Eq. (B7) appendix part B).

Cardiac Cycle (Tensor Gradient Φ_{PC} or F_{A_0C})

At a given growth time t_g, the LV fetal stress-free state P (Fig. 8) is subjected to the following deformations to simulate the cardiac cycle: (i) The cylindrical geometry of the LV at state P (or A_0) remains cylindrical at states $S(t)$, $A(t)$ and $C(t)$, (ii) The base of the fetal LV is only radially free to move and the axial extension is proportional to the distance of the plane from the base, (iii) a uniform simple torsion in a plane perpendicular to the Z axis is proportional to the distance of the plane from the base. From these assumptions, a same fiber runs always on a cylindrical shell and the unit vector in the fiber direction is given by $\mathbf{t}_H = \cos \gamma_H \mathbf{e}_{\Theta H} + \sin \gamma_H \mathbf{e}_{ZH}$, where γ_H is the radial distribution of the elevation angel at the arbitrary cardiac cycle state H.

From state P, the activation of muscle fibers is modeled as described previously (Section 4.2). The non-elastic transformation $\mathbf{\Phi}_{PA_0} = \mathbf{I}$ changes the material rheology without changing the geometry, then the LV undergoes three elastic deformations. The closure of the open configuration A_0 gives the state S, and from that state S, the fiber contraction produced by the active tension delivered by the fibers gives the state A. Finally the external load applied to state A gives the state C. Note that two virtual states (A_0 and S) are used to simulate the cardiac cycle.

With this model, the cardiac cycle is viewed as a global elastic transformation because $\mathbf{\Phi}_{PC} = \mathbf{F}_{A_0C}\mathbf{\Phi}_{PA_0} = \mathbf{F}_{A_0C}$. The following paragraphs formalize, at a fixed growth time, the governing equations of that elastic transformation $\mathbf{F}_{A_0C}$. Let the cylindrical coordinates in state P (or A_0) and $C(t)$ noted $(R = R_p, \Theta = \Theta_P, Z = Z_P)$ and $(r = R_C, \theta = \Theta_C, z = Z_C)$, respectively, for simplicity. Then the corresponding position vectors are

$$\mathbf{R} = R\mathbf{e_R} + Z\mathbf{e_Z} \quad \text{and} \quad \mathbf{r} + r\mathbf{e_r} + z\mathbf{e_z} \qquad (5a,b)$$

According to the above hypothesis and using the kinematics of the LV growth (Eqs. (4e–h)), the kinematics of the fetal LV during the cardiac cycle is described by:

$$r = r(R, t), \quad \theta = \frac{\pi}{\Theta_P^*}\Theta + \Psi(t)Z, \quad z = \Lambda(t)Z \qquad (5c-e)$$

where $R_{iP} \leq R \leq R_{ep}$, $-\Theta_P^* \leq \Theta \leq \Theta_P^*$, $-L_P \leq Z \leq 0$, $\Psi = \Psi_{PC} = \Psi_{P_0C}\alpha_Z^{-1}$ and $\Lambda = \Lambda_{PC} = \Lambda_{P_0C}\alpha_Z^{-1}$. The axial extension ratio and the LV twist by unit of LV length, at state Q relative to state H, are noted Λ_{HQ} and Ψ_{HQ}, respectively (H and Q are two arbitrary cardiac cycle states).

From Eqs. 5c–e and B6a–c (see appendix part B) we can derive the temporal evolution of the LV cavity volume at state C during the cardiac cycle (noted V_C):

$$V_C = \pi r_i^2 \Lambda L_P \quad \text{with} \quad L_P = \alpha_Z L_{P_0} \quad \text{and}$$
$$L_{P_0} = \Lambda_{P_0S_0}^{-1}L_{S_0} \qquad (6a-c)$$

where r_i is the internal LV radius at state C.

Let identify in this study the curvilinear coordinates $(\theta^1, \theta^2, \theta^3)$ to (r, θ, z). The base vectors, the components of the metric tensors in states P and C, as well as the invariants I_1 and I_4 are given in part A of the appendix. Moreover, the incompressibility of the material yields $det\,\mathbf{\Phi}_{PC} = 1$, or:

$$\frac{\partial r}{\partial R} = R\frac{\Theta_P^*}{\pi}(\Lambda r)^{-1} \qquad (7)$$

Associated to the cardiac cycle kinematics (Eqs. (5c–e)), the non zero components of the Cauchy stress tensor given by Eqs. (3a–e), are:

$$\tau_C^{11} = -p_C + 2\left(R\frac{\Theta_P^*}{\pi}(\Lambda r)^{-1}\right)^2\frac{\partial W}{\partial I_1} \qquad (8a)$$

$$\tau_C^{22} = -p_C r^{-2} + 2\left\{\left[\left(\frac{\Theta_P^*}{\pi}R\right)^{-2} + \Psi^2\right]\frac{\partial W}{\partial I_1}\right.$$
$$\left. + \left[\left(\frac{\Theta_P^*}{\pi}R\right)^{-1}\cos\gamma_p + \Psi\sin\gamma_p\right]^2\frac{\partial W}{\partial I_4}\right\} \qquad (8b)$$
$$+ \beta T^{(0)}r^{-2}\cos^2\gamma_C$$

$$\tau_C^{33} = -p_C + 2\Lambda^2\left(\frac{\partial W}{\partial I_1} + \sin^2\gamma_P\frac{\partial W}{\partial I_4}\right)$$
$$+ \beta T^{(0)}\sin^2\gamma_C \qquad (8c)$$

$$\tau_C^{23} = \tau_C^{32} = 2\Lambda\left\{\Psi\frac{\partial W}{\partial I_1} + \left[\left(\frac{\Theta_P^*}{\pi}R\right)^{-1}\cos\gamma_P\right.\right.$$
$$\left.\left. + \Psi\sin\gamma_P\right]\sin\gamma_P\frac{\partial W}{\partial I_4}\right\} \qquad (8d)$$
$$+ \beta T^{(0)}r^{-1}\cos\gamma_C\sin\gamma_C$$

where $\partial W/\partial I_1$ and $\partial W/\partial I_4$ can be easily derived from Eq. (3a–d). The elevation fiber angle γ_C at state C, which is needed to derive the components of the Cauchy stress tensor at the same state τ_C^{ij} (Eqs. (8a–d)), is given by (see appendix part B):

$$\gamma_C = \arctan\left\{\left[\left(\frac{\Theta_P^*}{\pi}R\right)^{-1}\cos\gamma_P + \Psi\sin\gamma_P\right]^{-1}r^{-1}\Lambda\sin\gamma_P\right\} \qquad (9)$$

Neglecting the inertia and the gravitational effects, the local equilibrium equation becomes $div\,\tau_C = \mathbf{0}$, or:

$$\frac{\partial\tau_C^{11}}{\partial r} + \frac{1}{r}\tau_C^{11} - r\tau_C^{22} = 0. \qquad (10)$$

The boundary conditions at state C for the present problem consist of a balance of forces and moments at the closed end of the cylinder (or at the apex, on $z = -L_C$) and specified tractions at the inner (or endocardium, on $r = r_i$) and outer surfaces (or epicardium, on $r = r_e$).

TABLE II Eleven cardiac cycle points where the simulations are run for the results presented in Fig. 10. V_{ed}: LV end-diastolic cavity volume, V_{es}: LV end-systolic cavity volume ($V_{es} = (1 - EF^*)V_{ed}$, where EF^* is the ejection fraction), ED: End-diastolic state, BE: Beginning ejection state, ES: End-systolic state, BF: Beginning filling state, β: Muscle activation amplitude ($0 \le \beta \le 1$), t: Cardiac cycle time, T_{cyc}: Cardiac cycle period

State	t/T_{cyc}	β	LV cavity volume
ED	0	0	V_{ed}
BE	0.06	0.5	V_{ed}
	0.155	0.625	$(3V_{ed} + V_{es})/4$
	0.25	0.75	$(V_{ed} + V_{es})/4$
	0.345	0.875	$(V_{ed} + 3V_{es})/4$
ES	0.44	1	V_{es}
	0.47	0.4	V_{es}
BF	0.5	0.1	V_{es}
	0.64	0.008	$(3V_{ed} + V_{es})/4$
	0.76	0.004	$(5V_{ed} + V_{es})/6$
	0.88	0.001	$(11V_{ed} + V_{es})/12$
ED	1	0	V_{ed}

For an internal pressure P_v and negligible external loads, these conditions are:

$$\int_{r_i}^{r_e} \tau_C^{33} r \, dr = \frac{1}{2} P_v r_i^2 \quad \text{on} \quad z = -L_C \quad (11a)$$

$$\int_{r_i}^{r_e} \tau_C^{23} r^3 dr = 0 \quad \text{on} \quad z = -L_C \quad (11b)$$

$$\tau_C^{11} = -P_v(t) \quad \text{on} \quad r = r_i \quad (11c)$$

$$\tau_C^{11} = 0 \quad \text{on} \quad r = r_e \quad (11d)$$

The Growth Law

As Lin and Taber [2] we used a linear relationship for the growth law, but we assumed that the growth rates (noted $\dot{\alpha}_i$ with $i = 1, 2, 3$ or $(\dot{\alpha}_R, \dot{\alpha}_\Theta, \dot{\alpha}_Z)$) depend of the mean physical components of the wall Cauchy stress tensor averaged through the space and during whole fetal cardiac cycle (noted $\sigma_{\langle j \rangle}$ with $j = 1, 2, 3, 4$ or $(\sigma_{\langle rr \rangle}, \sigma_{\langle \theta\theta \rangle}, \sigma_{\langle zz \rangle}, \sigma_{\langle \theta z \rangle})$)):

$$\dot{\alpha}_i = D_{ij}(\sigma_{\langle j \rangle} - \sigma_{\langle j \rangle}^*) \quad \text{with } i = 1, 2, 3, \\ \text{and } j = 1, 2, 3, 4 \quad (12)$$

where dot denotes growth time differentiation, and $\sigma_{\langle j \rangle}^* = (\sigma_{\langle rr \rangle}^*, \sigma_{\langle \theta\theta \rangle}^*, \sigma_{\langle zz \rangle}^*, \sigma_{\langle \theta \rangle}^*)$ are the growth equilibrium stresses or the mean physical components of the Cauchy stress tensor averaged through the ventricular wall and during the whole adult cardiac cycle. The constants D_{ij} are the growth rate coefficients (unit: $kPa^{-1}s^{-1}$) characterizing the contribution of jth Cauchy stress physical component on the growth in the ith direction. Note that $\dot{\alpha}_i > 0$, $\dot{\alpha}_i < 0$ and $\dot{\alpha}_i = 0$ means growth, resorption and growth-equilibrium in the i direction, respectively.

The relationship between the non-zero local physical stresses (noted σ_{ij}) and the components of the Cauchy stress tensor are: $\sigma_{rr} = \tau_C^{11}$, $\sigma_{\theta\theta} = r^2 \tau_C^{22}$, $\sigma_{zz} = \tau_C^{33}$, $\sigma_{\theta z} = r\tau_C^{23}$.

NUMERICAL RESULTS AND DISCUSSION

Computational Procedure

At given growth time t_g, the boundary problem (Eqs. 4(h–i), B7, 6(a–c), 7, 8(a–d), 9, 10, 11(a–d) and 12 for the unknowns $\tau_C^{11}, \tau_C^{22}, \tau_C^{33}, \tau_C^{23}, r, \gamma_C, p_C, \mathbf{P}_v, \Lambda$ and Ψ) was solved numerically on a Silicon Graphics Indy 5000 SC/180 Mhz using the International Mathematical Statistical Library (IMSL) routine NEQNS for nonlinear equation systems. First, we evaluated the growth-equilibrium stresses $\sigma_{\langle j \rangle}^*(j = 1, 2, 3, 4)$ by simulating the adult cardiac cycle. In a second step, state P_0 is computed by fixing the value of the opening angle $\Theta_{P_0}^{open}$ and inputing the knowledge of the geometry and the fiber organization of the FH at state S_0. Then the growth computation starts, and at each growing-time step the mechanical behavior of the LV FH simulated during the cardiac cycle. The growing-time step is chosen to be 1 week for our computations knowing that numerical simulations done with a growing-time step of 1 day give the same results.

For the adult and fetal life, we simulate the cardiac cycle at 4 points corresponding to the opening and closure of the valves for which we give the fiber-activation amplitudes: $\beta = 0$ at end-diastole, $\beta = 0.5$ at the beginning of ejection, $\beta = 1$ at end-systole and $\beta = 0.1$ at the beginning of filling (states noted ED, BE, ES and BF, respectively). We also give the period of filling phase, isovolumic contraction phase, ejection phase and isovolumic relaxation phase, which are respectively $0.5T_{cyc}$, $0.06T_{cyc}, 0.38T_{cyc}$ and $0.06T_{cyc}$ where T_{cyc} is the cardiac cycle period. In order to compare our numerical results with some experimental data coming form the literature, we ran simulations at eleven points of the cardiac cycle. For each point we know the values of the normalized cardiac cycle, the amplitude of activation and the cavity volume (Tab. II).

Adult Heart

The equations describing the cardiac cycle of the human fetal LV (Eqs. 6(a–b), 7, 8(a–d), 9, 10 and 11(a–d) can also be used to simulate the cardiac cycle of the human adult LV by letting $\alpha_R = \alpha_\Theta = \alpha_z = 1$ and by fixing the value of $(\Theta_P^{open}$ or $\Theta_P^*)$. We were unable to find values for the opening angle of the human adult LV, therefore we used the data of Rodriguez et al. [35] obtained on the mature rat LV ($\Theta_P^{open} = 45°$ or $\Theta_P^* = 157.5°$). The previous system is solved for the unknowns $\tau_C^{11}, \tau_C^{22}, \tau_C^{33}, \tau_C^{23}, r, \gamma_C, p_C, \mathbf{P}_v, \Lambda,$ and Ψ. For the passive unloaded physiological state of the adult LV (noted C_0), corresponding to states C when myocardium is passive

with zero cavity pressure (Fig. 8), we use the following cavity volume, internal and external radii: $V_{C_0} = 64.34$ ml, $R_{iC_0} = 1.6$ cm, $R_{eC_0} = 2.55$ cm [36,37]. We were unable to find values for the elevation angle in the human adult LV myocardium, but based on the work of Streeter [8] done on adult dog we assumed a linear radial distribution of the fiber elevation angel γ_{C_0} going from 70° at the endocardium to $-70°$ at the epicardium. The adult simulation use an ejection fraction of 0.5 with an end-diastolic volume of 192 ml [38]. In a first step state P (or A_0) is computed by letting the open angle $\Theta_P^{open} = 45°$, then simulation of the cardiac cycle is performed. The passive material parameters are adapted to agree with the experiments of Demer and Yin [39], and Lin and Yin [40] done on the passive myocardium : $a = 0.1$ kPa, $b = 1.5$, $a_f = 0.4$ kPa, $b_f = 2$. The active material parameters are adapted to agree with the physiological pressure-volume relation obtained on normal human adult LV [36,38]: $c_f = 70$ kPa, $d_f = 1.2$, $T_0 = 35$ kPa. From our calculations we obtained $\sigma_{\langle rr \rangle}^* = -2.84$ kPa, $\sigma_{\langle \theta\theta \rangle}^* = 21.37$ kPa, $\sigma_{\langle zz \rangle}^* = 10.00$ kPa and $\sigma_{\langle \theta z \rangle}^* = 2.61$ kPa.

Normal Fetal Heart Growth

As said before, the geometry of the 14 weeks LV was chosen as the growth passive reference state P_0 with $\Theta_{P_0}^{open} = 0°$. In fact we assumed that there is no residual stress in the human LV at the beginning of the fetal period [41] and that states P_0 and S_0 are the same ($\mathbf{F}_{P_0 S_0} = \mathbf{I}$). The values of the cavity volume, the internal and external radii, the internal long axis and the transmural distribution of γ at state S_0 are based on anatomical data of normal human FH measured by Ohayaon *et al.* [1]: $V_{S_0} = 8.04 \times 10^{-2}$ ml, $R_{iS_0} = 0.16$ cm, $R_{eS_0} = 0.28$ cm and $\gamma_{S_0}(\rho) = \gamma_{nor.}(\rho)$ where $\gamma_{nor.}$ is defined in Section 3. We began the computational at 14 weeks by letting $\mathbf{\Phi}_{P_0 P}^{grow} = \mathbf{I}$ (or $\alpha_R = \alpha_\Theta = \alpha_Z = 1$), then the next α_i were calculated from Eq. (12).

Friedman [42] found that developed tension is lesser in fetal lambs than in adult sheep. This finding supports the idea of decreased contractility in the fetus. Because the FH was composed of only 30% myofibrils as opposed to the adult heart with 60%, Friedman suggested that the contractility of individual sarcomeres was similar in fetal and adult hearts, but there was simply more contractile material in adult hearts. Based on the Friedman's conclusions, we kept the same adult passive rheological parameters a, b, a_f, b_f and d_f for the FH, but we use a lower values of $c_f = 20$ kPa and $T_0 = 15$ kPa. These last data are adapted to agree with the mean arterial blood systolic pressure measured at the beginning of the fetal sheep period [43] which is in the order of 25 mmHg. Moreover, we assume that the muscle properties of the heart do not change during human fetal development. Obviously, this assumption may not be valid, but few data are available to determine how these properties change. Concerning the passive properties of the myocardium it is known that the density of collagen in the myocardium increases slightly

with the gestational age, in fact the main change occurs during postnatal heart development [44].

Again, we were unable to find values for the end-diastolic and end-systolic LV pressures during human fetal life in the literature and therefore regard the LV cavity pressure as a free parameter. Instead, we use the measured end-diastolic ventricular volume as an input of the model (Eq. (2a)). Moreover, the ejection fraction (EF*) of fetal LV is near constant and equal to 0.6 [16,45].

In our growth law we assume that the normal stresses σ_{rr}, $\sigma_{\theta\theta}$ and σ_{zz} contribute in an equal manner to the tissue growth in their direction ($D_{11} = D_{22} = D_{33}$) which is consistent with the observed homothetic growth of the myocardium [46]. Similarly, we assume that the normal stresses influence the growth in their perpendicular directions in an identical manner ($D_{12} = D_{21} = D_{13} = D_{31} = D_{23} = D_{32}$) and that the shear stress $\sigma_{\theta z}$ regulates equally the circumferential and longitudinal growth ($D_{24} = D_{34}$). With such assumptions our growth law depends only on 4 parameters D_{11}, D_{12}, D_{24} and D_{14}. Because the growth cells are very sensitive to the shear stress [47] which is small compared to the circumferential stress, we have chosen a large amplitude for the coefficients D_{i4} ($i = 1, 2, 3$). The four growth-rate coefficients D_{ij} are adapted to agree with the measured variations with gestational age of internal long axis, equatorial radii and LV wall mass (Figs. 3–6): $D_{11} = D_{22} = D_{33} = -6.5 \times 10^{-3}$ kPa^{-1}s^{-1}, $D_{12} = D_{21} = D_{13} = D_{31} = D_{23} = D_{32} = -4.2 \times 10^{-3}$ kPa^{-1}s^{-1}, $D_{24} = D_{34} = 30 \times 10^{-3}$ kPa^{-1}s^{-1} and $D_{14} = -10 \times 10^{-3}$ kPa^{-1}s^{-1}.

Figure 9 shows computed LV pressure–volume loops of the normal heart during fetal development from 20 to 40 weeks of gestation. It appears that the slope of the Growth End–Diastolic Pressure–Volume Curve
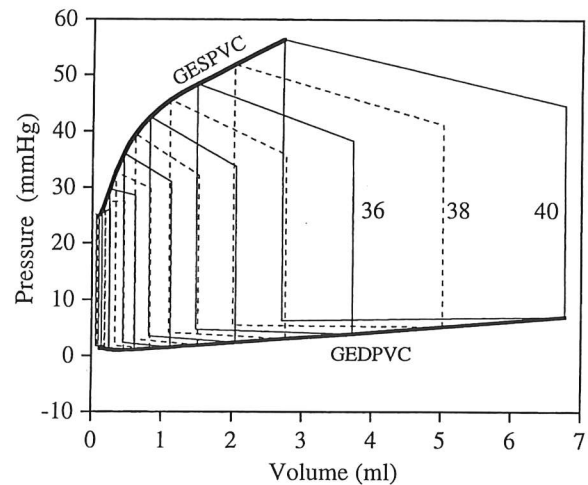

FIGURE 9 Numerical simulation predicting the evolution of the LV pressure-volume loops during normal fetal life from 14 to 40 weeks of gestation. To have a better view of the pressure-volume loops evolution, the cardiac cycle is presented every two weeks and only with the 4 points corresponding to the opening and closure of the valves. The numbers indicate the gestational age. GEDPVC: is the growth end-diastolic pressure-volume curve, GESPVC: is the growth end-systolic pressure-volume curve. (1 mmHg = 0.13 kPa).
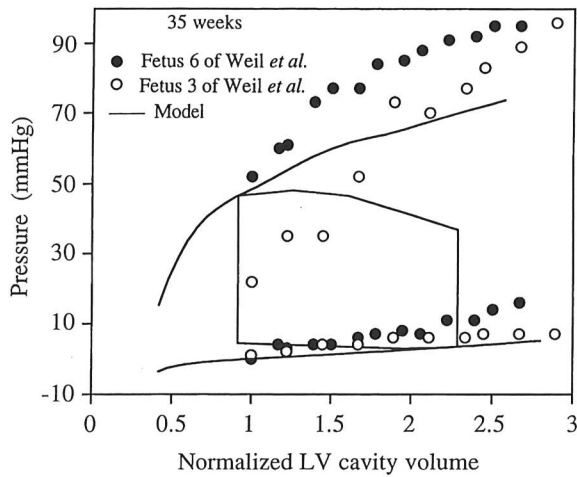
FIGURE 10 Comparison between computed values for a FH of 35 weeks of gestation and experimental data of a fetal lamb heart at similar development. The plain lines are the computed LV pressure-volume loop, end-diastolic and end-systolic pressure–volume relations for the human fetal heart of 35 weeks of gestation. Open and closed circles are the experimental data, of 2 isolated fetal lamb hearts between 129 and 135 days of gestation, given the end-diastolic and end-systolic pressure-volume relations (Weil *et al.*, 1993). The volume is normalized by the passive unloaded physiological LV cavity volume. (1 mmHg = 0.13 kPa).
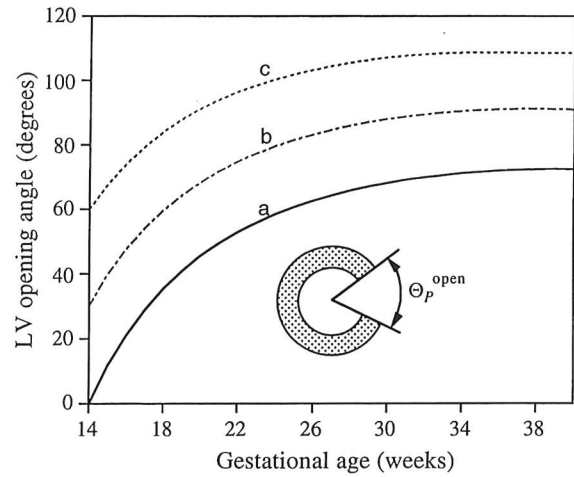

FIGURE 11 Effect of the initial opening angle $\Theta_{P_0}^{open}$ on the predicted evolution of the LV opening angle Θ_P^{open} during normal fetal life from 14 to 40 weeks of gestation. Curve a: $\Theta_{P_0}^{open} = 0°$ this corresponds to a simulation where no residual stresses are assumed at the beginning of the fetal period. Curve b: $\Theta_{P_0}^{open} = 30°$, Curve c: $\Theta_{P_0}^{open} = 60°$.

(noted GEDPVC in Fig. 9) is almost constant, while the slope of the Growth End-Systolic Pressure-Volume Curve (noted GESPVC in Fig. 9) decreases with gestational age. The calculated end-systolic LV pressures (25 mmHg, 35 mmHg and 55 mmHg respectively for the FH of 20, 30 and 40 weeks) are in the order of the measured mean arterial blood pressure during fetal sheep period [43]. For the end-diastolic LV pressures our calculations (2.5 mmHg, 2.5 mmHg and 7 mmHg respectively for the FH of 20, 30 and 40 weeks) are in agreement with the passive pressure-volume curves obtained on fetal sheep ventricles [48]. Weil *et al.* [49] have measured the end-diastolic and end-systolic LV pressure-volume relationship on 10 isolated fetal lamb hearts of 129 to 135 days of gestation. Knowing that the term gestation for sheep is between 145 and 155 days, we have compared their measurements with the numerical results obtained for a human FH at similar development which is 35 weeks of gestation. The comparison shows a good agreement between experimental data and computed values (Fig. 10).

Residual stress can also be predicted with such a model. Figure 11 (curve a) gives computed opening angle of the LV during fetal life from 14 to 40 weeks of gestation. This result shows that the opening angle of the fetal LV increases rapidly at the first weeks of the fetal life and slowly near neonatal age with about 70° at 40 weeks of gestational age. To date, there is no available experimental data of residual stresses and strains to compare with our numerical results, for the human fetal hearts. Actually, the prediction of the residual stresses and strains could be also obtained with growth laws based on other assumptions [50].

The shape of the computed transmural distributions of end-systolic fiber stress are very similar during fetal growth

and at the adult age, but the main change of amplitude seems to occur during the postnatal period (Fig. 12).

The assumption of zero residual stress at the beginning of the fetal period $\left(\Theta_{P_0}^{open} = 0°\right)$ is not supported by Taber's *et al.* [51] data. The average opening angle measured by these authors at stage 24 of LV chick embryo (approximately 4.5 days of a 21-day incubation period) is $74° \pm 7°$. To evaluate the effects of the initial opening angle $\Theta_{P_0}^{open}$ on the structural and functional development of the normal human fetal LV, we have made some additional computations by changing only (with $\Theta_{P_0}^{open} = 30°$ and 60°). Compared to the simulation with $\Theta_{P_0}^{open} = 0°$, the increase of the initial opening angle gives almost no change on the evolution of the myocardial mass and end-diastolic cavity length, during fetal life. At end-diastole, the main changes occur on the evolutions of the wall thickness (which decreases), inner radius
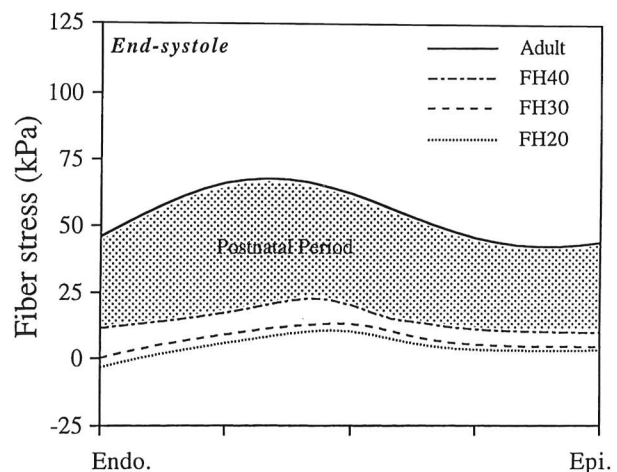

FIGURE 12 Computed transmural distributions of end-systolic fiber stress for the normal hearts, at 20 (curve FH20), 30 (curve FH30) and 40 (curve FH40) weeks of gestation and at the adult age. Edo.: Endocardium, Epi.: Epicardium.

(which increases), opening angle Θ_P^{open} (which increases, see Fig. 11), and on the end-diastolic and end-systolic pressures (which increase), during fetal period. Thus, with this model and compared to the simulation with no initial residual stress, an initial non zero residual stress gives a thinner wall and in the same time decreases the compliance of the passive fetal LV and improves the active LV performance by generating higher systolic pressures within physiological range.

As a final remark, we again emphasize that the paucity of experimental data for the developing human FH forced us to make a number of realistic assumptions that cannot be validated at present. One of the major limitation of our model comes from the fact that we did not take into account the fiber penetration angle that we measured [1], because of the increase of complexity of the mathematical expression of the model. An obvious solution of the latter problem will be the use of the finite element method which is mathematically more complex and requires powerful computing resources. Nevertheless the presented echo-cardiographic measurements and the proposed mechanical model based on a global growth law which can predict reasonably the growth of the normal human LV during fetal life, could be useful in fetal cardiology to assess the functional capacities of the fetal heart. These conclusions await further data on microstructure and material properties of the human fetal heart during development.

References

[1] Ohayaon, J., Usson, Y., Jouk, P.S. and Cai, H. (1999). Fiber Orientation in Human Fetal Heart and Ventricular Mechanics: a Small Perturbation Analysis, *Computer Methods in Biomechanics and Biomedical Engineering*, 2, 83–105.

[2] Lin, I.E. and Taber, L.A. (1995). A Model for Stress-Induced Growth in the Developing Heart, *Journal of Biomechanical Engineering*, 117, 343–349.

[3] Zak, R. (1984). *Growth of the Heart in Health and Disease*, Raven Press.

[4] Clark, E.B. and Takao, A. (1990). *Developmental Cardiology, Morphogenesis and Function*, Futura Publishing.

[5] Rodriguez, E.K., Hoger, A. and McCulloch, A.D. (1994). Stress-Dependent Finite Growth in Soft Elastic Tissues, *Journal of Biomechanics*, 27, 455–467.

[6] Hort, W. (1960). Makroskopische und Mikrometrische Untersuchungen am Kyokard Verschieden Stark Geflüliter Linker Kammern, *Virchows Arch. Pathol. Anat.*, 33, 523–564.

[7] Torrent-Guasp, F. (1973). *The Cardiac Muscle*, Fundaciòn Juan March, Madrid, Spain.

[8] Streeter, D.D. (1979). Gross Morphology and Fiber Geometry of the Heart. In: *Handbook of Physiology* (Berne, R.M. *et al.*, Eds.), American Physiological Society, Bethesda, MD, 1, Section 2, 61–112.

[9] Greenbaum, R.A., Ho, S.Y., Gibson, D.G., Becker, A.E. and Anderson, R.H. (1981). Left Ventricular Fibre Architecture in Man, *British Heart Journal*, 45, 248–263.

[10] Nielsen, P.M.F., LeGrice, I.J., Smaill, B.H. and Hunter, P.J. (1991). Mathematical Model of Geometry and Fibrous Structure of the Heart, *American Journal of Physiology*, 260, H1365–H1378.

[11] Jouk, P.S., Usson, Y., Michalowicz, G. and Grossi, L. (2000). Three-dimensional cartography of the pattern of the myofibres in the second trimester fetal human heart, *Anat. Embryol.*, 202, 103–118.

[12] Sanchez-Quintana, D., Garcia-Martinez, V., Climent, V. and Hurle, J.M. (1995). Morphological Changes in the Normal Pattern of Ventricular Myoarchitecture in the Developing Human Heart, *The Anatomical Record*, 243, 483–495.

[13] Cai, H. (1998). Constitutive equations describing finites deformations of the active myocardium: application to the mechanics of human heart and to the fetal growth, *Ph. D. Thesis,* University of Savoie, France.

[14] Jouk, P.S., Usson, Y., Michalowicz, G. and Grossi, L. (2000). Three-dimensional cartography of the pattern of the myofibres in the second trimester fetal human heart, *Anat. Embryol.*, 202, 103–118.

[15] Azancot, A., Caudell, T., Allen, H.D., Horowitz, S., Sahn, S., Stoll, C., Theis, C., Valdez-Cruz, L.M. and Golberg, S.J. (1983). Analysis of Ventricular Shape by Echocardiography in Normal Fetuses, Newborns and Infants, *Circulation*, 68, 1901–1911.

[16] Schmidt, K.G., Silverman, N.H. and Hoffman, J.I.E. (1995). Determination of Ventricular Volumes in Human Fetal Hearts by Two-Dimensional Echocardiography, *The American Journal of Cardiology*, 76, 1313–1316.

[17] McCaffrey, F.M. and Sherman, F.S. (1997). Prenatal Diagnosis of Severe Aortic Stenosis, *Pediatric Cardiology*, 18, 276–281.

[18] Schmidt, K.G., Silverman, N.H., Van Hare, G.F., Hawkins, J.A., Cloez, J.L. and Rudolph, A.M. (1990). Two-Dimensional Echocardiographic Determination of Ventricular Volumes in the Fetal Heart, *Circulation*, 81, 325–333.

[19] Schmidt, K.G., de Araujo, L.M.L. and Silverman, N.H. (1988). Evaluation of the Fetal Heart by Echocardiography. I. Structural of Functional Abnormalities, *American Journal of Cardiology Imaging*, 2, 57–76.

[20] Usson, Y., Parazza, F., Jouk, P.S. and Michalowicz, G. (1994). Method for the Study of the Three-Dimensional Orientation of Myocardial Cells by Means of Confocal Scanning Laser Microscopy, *Journal of Microscopy*, 174, 101–110.

[21] Jouk, P.S., Usson, Y., Michalowicz, G. and Parazza, F. (1995). Mapping of the Orientation of Myocardial Cells by Means of Polarized Light and Confocal Scanning Laser Microscopy, *Microscopy Research and Technique*, 30, 480–490.

[22] Cai, H., Usson, Y., Jouk, P.S. and Ohayon, J. (1999). Fiber Orientation in Mid-Gestation human Fetal Heart and Ventricular Mechanics, *Innov. Techn. Biol. Med.*, 20, 67–83.

[23] van Campen, D.H., Huyghe, J.M., Bovendeerd, P.H.M. and Arts, T. (1994). Biomechanics of the Heart Muscle, *European Journal of Mechanics, A/Solids*, 13, 19–41.

[24] Chadwick, R.S. (1982). Mechanics of the Left Ventricle, *Biophysical Journal*, 39, 279–288.

[25] Ohayon, J. and Chadwick, R.S. (1988). Effects of Collagen Microstructure on the Mechanics of the Left Ventricle, *Biophysical Journal*, 54, 1077–1088.

[26] Humphrey, J.D. and Yin, F.C.P. (1989). Constitutive Relations and Finite Deformations of Passive Cardiac Tissue II: Stress Analysis in the Left Ventricle, *Circulation Research*, 65, 805–817.

[27] Guccione, J.M., Waldman, L.K. and McCulloch, A.D. (1993). Mechanics of Active Contraction in Cardiac Muscle: Part II-Cylindrical Models of the Systolic Ventricle, *Journal of Biomechanical Engineering*, 115, 82–90.

[28] Hunter, P.J. (1995). Myocardial Constitutive Laws for Continuum Mechanics Models of the Heart. In: *Molecular and Subcellular Cardiology: Effects of Structure and Function* (Sideman, S. and Beyar, R., Eds.), Plenum Press, 30, 303–318.

[29] Taber, L.A. (1991). On a Nonlinear Theory for Muscle Shells: Part II—Application to the Beating Left Ventricle, *Journal of Biomechanical Engineering*, 113, 63–71.

[30] Fung, Y.C. (1965). *Foundation of Solid Mechanics*, Prentice-Hall.

[31] Green, A.E. and Zerna, W. (1992). *Theoretical Elasticity*, Dover Publication.

[32] Fung, Y.C. (1997). *Biomechanics: Circulation*, Springer.

[33] Anversa, P., Olivetti, G. and Loud, A.V. (1980). Morphometric Study of Early Postnatal Development in the Left and Right Ventricular Myocardium of the Rat: I-Hypertrophy, Hyperplasia, and Binucleation of Myocytes, *Circulation Research*, 46, 495–502.

[34] Skalak, R. (1981). Growth as a Finite Displacement Field, *Proceedings of the IUTAM Symposium on Finite Elasticity* (Carlson, D.E. *et al.,* Eds.), Martinus Nijhoff Publihers, The Hauge, pp. 347–355.

[35] Rodriguez, E.K., Omens, J.H., Waldman, L.K. and McCulloch, A.D. (1993). Effect of Residual Stress on Transmural Sarcomere Length Distributions in Rat Left Ventricle, *American Journal of Physiology*, **264**, H1048–H1056.

[36] Ingel, N.B., Daughters, G.T., Stinson, E.B., Alderman, E.L. and Miller, D.C. (1990). Three-Dimensional Left Ventricular Midwall dynamics in the Transplanted Human Heart, *Circulation*, **81**, 1837–1848.

[37] Ingel, N.B., Daughters, G.T., Nikolic, A.D., Moon, M.R., Bolger, A.F., Komeda, M., Derby, G.C., Yellin, E.L. and Miller, D.C. (1996). Left Ventricular Diastolic Suction with Zero Left Atrial Pressure in Open-Chest Dogs, *American Journal of Physiology*, **270**, H1217–H1224.

[38] Parmley, W.W. and Talbot, L. (1979). Heart as a Pump, In: *Handbook of Physiology* (Berne R.M. *et al.,* Eds.), American Physiological Society, Bethesda, MD, **1**, Section 2.

[39] Demer, L. and Yin, F.C.P. (1983). Passive Biaxial Mechanical Properties of Isolated Canine Myocardium, *Journal of Physiology* (London), **339**, 615–630.

[40] Lin, D.H.S. and Yin, F.C.P. (1998). A Multiaxial Constitutive Law for Mammalian Left Ventricular Myocardium in Steady-State Barium Contracture or Tetanus, *Journal of Biomechanical Engineering*, **120**, 504–517.

[41] Laurini, R., Private Communication, Institute of Pathology, Lausanne, Switzerland (1998).

[42] Friedman, W.F. (1972). The Intrinisic Physiologic Properties of the Developing Heart, *Progress in Cardiovascular Diseases*, **15**, 87–111.

[43] Hanson, M.A. (1993). The Control of Heart Rate and Blood Pressure in the Fetus: Theoretical Consideration. In: *Fetus and Neonate Physiology and Clinical Applications: The Circulation* (Hanson, M.A. *et al.*, Eds.), Cambridge University Press, **1**, 1–22.

[44] Borg, T.K., Nakagawa, M., Carve, W., Terracio, L. (1995). Overview: Extracullular Matrix, Receptors, and Heart Development. In: *Development Mechanisms of Heart Disease* (Clark, E.B. *et al.*, Eds.), Futura Publishing Company, 175–184.

[45] Ibarra-Polo, A.A., Guiloff, E. and Gomez-Rogers, C. (1972). Fetal Heart Rate Throughout Pregnancy, *Journal Obstetric Gynecology*, **113**, 814–818.

[46] Anversa, P., Ricci, R. and Olivetti, G. (1986). Quantitative Structural Analysis of the Myocardium during Physiologic Growth and Induced Cardiac Hypertrophy: a Review, *J. Am. Coll. Cardiol.*, **7**, 1140–1149.

[47] Brutsaert, D.L. and Andries, L.J. (1992). The endocardial endothelium, *American Journal of Physiology*, **263**, H985–1002.

[48] Thornburg, K.L., Morton, M.J. (1993). Growth and Development of the Heart. In: *Fetus and Neonate Physiology and Clinical Applications: The Circulation* (Hanson, M.A. *et al.*, Eds.), Cambridge University Press, **1**, 137–159.

[49] Weil, S.R., Russo, P.A., Heckman, J.L., Balsara, R.K., Pasiecki, V. and Dunn, J.M. (1993). Pressure-Volume Relationship of the Fetal Lamb Heart, *Ann. Thorac. Surg.*, **55**, 470–475.

[50] Taber, L.A. (1995). Biomechanics of growth, remodeling, and morphogenesis, *Appl. Mech. Rev*, **48**(8), 487–545.

[51] Taber, L.A., Hu, N., Pexieder, T., Clark, E.B. and Keller, B.B. (1993). Residual Strain in the Ventricle of the Stage 16–24 Chick Embryo, *Circulation Research*, **72**, 455–462.

APPENDIX

(A) Metric Tensors in States P and C, Invariants I_1 and I_4, Lagrange Strains at State C Referred to the End Diastolic State D

Metric Tensors in States P and C

The covariant base vectors in states P and C, respectively, are $\mathbf{G_i} = \mathbf{R}_{,i}$ and $\mathbf{g_i} = \mathbf{r}_{,i}$, where $A, i = \partial A / \partial \theta^i$ ($i = 1, 2, 3$) with $(\theta^1, \theta^2, \theta^3) = (r, \theta, z)$. The contravariant base

vector are defined by the relation $\mathbf{G_i} \cdot \mathbf{G^j} = \mathbf{g_i} \cdot \mathbf{g^j} = \delta_i^j$, with δ_i^j being the Kroenecker delta. The usual summation convention on repeated indices is used throughout this paper. Substituting the Eqs. (5c–e) into previous equations gives the four bases:

$$\mathbf{G_1} = \frac{\partial R}{\partial r}\mathbf{e_R} \quad \mathbf{G_2} = \frac{\Theta_P^*}{\pi}R\mathbf{e_\Theta}$$

$$\mathbf{G_3} = -\Lambda^{-1}\left(\frac{\Theta_P^*}{\pi}R\Psi\mathbf{e_\Theta} - \mathbf{e_Z}\right) \tag{A1a–c}$$

$$\mathbf{G^1} = \frac{\partial r}{\partial R}\mathbf{e_R} \quad \mathbf{G^2} = \left(\frac{\Theta_P^*}{\pi}R\right)^{-1}\mathbf{e_\Theta} + \Psi\mathbf{e_Z} \tag{A1d–f}$$

$$\mathbf{G^3} = \Lambda\mathbf{e_Z}$$

$$\mathbf{g_1} = \mathbf{e_r} \quad \mathbf{g_2} = r\mathbf{e_\theta} \quad \mathbf{g_3} = \mathbf{e_z} \tag{A1g–i}$$

$$\mathbf{g^1} = \mathbf{e_r} \quad \mathbf{g^2} = r^{-1}\mathbf{e_\theta} \quad \mathbf{g_3} = \mathbf{e_z} \tag{A1j–l}$$

Invariants I_1 and I_4

The components of the metric tensors in states P and C, respectively, are $G_{ij} = \mathbf{G_i} \cdot \mathbf{G_j}$, $G^{ij} = \mathbf{G^i} \cdot \mathbf{G^j}$ and $g_{ij} = \mathbf{g_i} \cdot \mathbf{g_j}$, $g^{ij} = \mathbf{g^i} \cdot \mathbf{g^j}$. The covariant Lagrange strain components are $E_{ij} = \mathbf{G_i} \cdot \mathbf{E}_{PC}$ $\mathbf{G_j} = (1/2)(g_{ij} - G_{ij})$ and the two invariants I_1 and I_4 are:

$$I_1 = G^{ij}g_{ij} = G^{ij}(2E_{ij} + G_{ij}),$$

$$I_4 = g_{ij}t_P^i t_P^j = (2E_{ij} + G_{ij})t_P^i t_P^j \tag{A2a, b}$$

where $t_P^i (i = 1, 2, 3)$ are the components of the unit vector in fiber direction at state P (noted $\mathbf{t_P}$) in the base $\mathbf{G_i} (i = 1, 2, 3)$ or $\mathbf{t}_P = t_P^i \mathbf{G_i}$.

Finally from Eqs. (A2a, b) we obtain the form of the invariant derivatives:

$$\frac{\partial I_1}{\partial E_{ij}} = 2G^{ij}, \quad \frac{\partial I_4}{\partial E_{ij}} = 2t_P^i t_P^j \tag{A3a, b}$$

useful to define $(\partial W / \partial E_{ij}) = (\partial W / \partial I_1)(\partial I_1 / \partial E_{ij}) + (\partial W / \partial I_4)(\partial I_4 / \partial E_{ij})$ himself needed to derive the components of the Cauchy stress tensor Eqs. (8a–d).

Physical Lagrange Strain Components at State C Referred to the End Diastolic State

In measuring Lagrange strains in the canine LV at midwall, some authors used end diastole as reference state (noted state D). Following, we derive the relation between these strain components and those referred to the passive stress-free state P (Fig. 9).

Lagrange stain components at states C and D relative to state P are, respectively:

$$(E_{ij})_{PC} = \frac{1}{2}[g_{ij} - G_{ij}] \quad \text{and}$$

$$(E_{ij})_{PC} = \frac{1}{2}[(g_{ij})_D - G_{ij}] \tag{A4a, b}$$

where $(g_{ij})_D$ are the components of the metric tensors in state D.

Lagrange strain components at state C relative to state D are given by $(E_{ij})_{DC} = \frac{1}{2}[g_{ij} - (g_{ij})_D]$. This last equation with Eqs. (A4a, b) yields

$$(E_{ij})_{DC} = (E_{ij})_{PC} - (E_{ij})_{PD} \tag{A5}$$

Finally, using the Eqs. (A4a, b), (A5) and the expression of the physical Lagrange strain components at state C relative to state D given by $(E_{\langle ij\rangle})_{DC} = (E_{ij})_{DC}[(g_{ii})_D \times (g_{jj})_D]^{-1/2}$, yields

$$(E_{\langle ij\rangle})_{DC} = \frac{(E_{ij})_{PC} - (E_{ij})_{PD}}{\{[G_{ii} + 2(E_{ii})_{PD}][G_{jj} + 2(E_{jj})_{PD}]\}^{(1/2)}} \tag{A6}$$

(B) Fiber Orientation in States S_0, P_0, P and C

According to our assumptions, a helicoidal fiber running on a cylindrical surface in state S_0 remains always on a cylindrical surface in states P_0, P and C. Therefore the unit vectors in the fiber direction in states S_0, P_0, P and C are:

$$\mathbf{t}_Q = \cos\gamma_Q \mathbf{e}_{\Theta Q} + \sin\gamma_Q \mathbf{e}_{ZQ} \quad \text{with}$$

$$Q = S_0, P_0, P \quad \text{or} \quad C \tag{B1a-c}$$

If we note $\mathbf{dX}_Q$ the infinitesimal fiber length vector at state Q of amplitude l_Q, then $\mathbf{dX}_Q = l_Q\mathbf{t}_Q$ where $Q = S_0, P_0, P$ or C.

Relation Between the Elevation Angles in States P_0, P and C

Knowing the two non elastic deformation gradient tensors $\Phi_{P_0P}^{\text{grow}}$ (Eq. (4a)) and Φ_{PC} (derived from Eqs. (5c–e)):

$$\Phi_{PC} = \frac{\partial r}{\partial R}\mathbf{e}_{R_C}\otimes\mathbf{e}_{R_P} + r\left(\frac{\Theta_P^*}{\pi}R\right)^{-1}\mathbf{e}_{\Theta_C}\otimes\mathbf{e}_{\Theta_P}$$

$$+ r\Psi\mathbf{e}_{\Theta_C}\otimes\mathbf{e}_{Z_P} + \Lambda\mathbf{e}_{Z_C}\otimes\mathbf{e}_{Z_P} \tag{B2}$$

we are able to found the expression of $\mathbf{t}_P$ and $\mathbf{t}_C$ because $\mathbf{dX}_P = \Phi_{P_0P}^{\text{grow}}\mathbf{dX}_{P_0}$ and $\mathbf{dX}_C = \Phi_{PC}\,\mathbf{dX}_P$:

$$\mathbf{t}_P = l_{P_0}l_P^{-1}\Phi_{P_0P}^{\text{grow}}\mathbf{t}_{P_0}$$

$$= l_{P_0}l_P^{-1}(\alpha_\Theta\cos\gamma_{P_0}\mathbf{e}_{\Theta P} + \alpha_Z\sin\gamma_{P_0}\mathbf{e}_{ZP}) \tag{B3a}$$

$$\mathbf{t}_C = l_Pl_C^{-1}\Phi_{PC}\mathbf{t}_P$$

$$= l_Pl_C^{-1}\left\{r\left[\left(\frac{\Theta_P^*}{\pi}R\right)^{-1}\cos\gamma_P + \Psi\sin\gamma_P\right]\mathbf{e}_{\Theta C}\right. \tag{B3b}$$

$$\left. +\Lambda\sin\gamma_P\mathbf{e}_{ZC}\right\}$$

Therefore, the Eqs. (B3a, b) and (B1a–c) give the relation between γ_P and γ_{P_0} (Eq. (4i)) as well as the relation between γ_C and γ_P (Eq. (9)).

From Eqs. (B1a–c) and (A1) we can write the vectors $\mathbf{t}_P$ and $\mathbf{t}_C$ in the bases $\mathbf{G}_i$ and $\mathbf{g}_i$ ($i = 1, 2, 3$), respectively:

$$\mathbf{t}_P = t_P^i\mathbf{G}_i$$

$$= \left[\left(\frac{\Theta_P^*}{\pi}R\right)^{-1}\cos\gamma_p + \Psi\sin\gamma_p\right]\mathbf{G}_2$$

$$+ \Lambda\sin\gamma_p\mathbf{G}_3 \tag{B4}$$

$$\mathbf{t}_C = t_C^i\mathbf{g}_i = r^{-1}\cos\gamma_C\mathbf{g}_2 + \sin\gamma_C\mathbf{g}_3 \tag{B5}$$

This last equation (Eq. B5) is used to derive the components of the cauchy stress tensor (Eqs. 8a–d).

Relation Between the Elevation Angles in States P_0 and S_0

The kinematics of the elastic transformation from state P_0 to state S_0 is given by:

$$R_{S_0} = R_{S_0}(R_{P_0}, t), \quad \Theta_{S_0} = \frac{\pi}{\Theta_{P_0}^*}\Theta_{P_0},$$

$$Z_{S_0} = \Lambda_{P_0S_0}Z_{P_0} \tag{B6a-c}$$

From such equations, we can derive, as previously, the elastic deformation gradient $\mathbf{F}_{P_0S_0}$, and the relation between the two unit vectors $\mathbf{t}_{S_0}$ and $\mathbf{t}_{P_0}$ because $\mathbf{dX}_{S_0} = \mathbf{F}_{P_0S_0}\mathbf{dX}_{P_0}$. Therefore the relation between γ_{S_0} and γ_{P_0} is:

$$\tan\gamma_{P_0} = (\Lambda_{P_0S_0}\Theta_{P_0}^*R_{P_0})^{-1}\pi R_{S_0}\tan\gamma_{S_0} \tag{B7}$$